A Variational Adjoint Approach on Wide-Angle Parabolic Equation for Refractivity Inversion

Uygar Karabaş, Youssef Diouane, Rémi Douvenot

A Variational Adjoint Approach on Wide-Angle Parabolic Equation for Refractivity Inversion

Uygar Karabaş, Youssef Diouane, and Rémi Douvenot

***Abstract*—Radar systems performance under anomalous propagation conditions can be predicted if the atmosphere is properly known. This paper introduces a tomographic approach to estimate refractivity in the troposphere with an adjoint-based inversion method. A new adjoint model is developed for the two-dimensional wide-angle parabolic equation using variational adjoint approach, to invert refractivity from phaseless data measured with an array of radio receivers in open-sea environment. The obtained adjoint model is validated considering propagation through range-independent medium over flat perfectly-electric-conducting surface at horizontal polarization. The ill-posedness of the regarded inverse problem is shown with the optimization landscapes. The parametric study indicates the potential use of this method as a refractivity gradient retrieval system under certain circumstances.**

***Index Terms*—Refractivity inversion, inverse problem, wide-angle parabolic equation, adjoint model.**

I. Introduction

NON-STANDARD refractive index variations cause performance anomalies for maritime communication and surveillance platforms [1]. Prediction of tropospheric refractivity in abnormal propagation conditions is crucial for survey radars because these conditions create blind zones, increase clutter level, alter detection range and cause range-altitude errors [2]. Although accurate radar coverage estimation methods exist taking refractivity as input [3]–[7], abnormal conditions are poorly quantified in practical sense [8]. It is necessary to quantify the refractivity over spatial extent of the platform for the entire operation time dynamically with robust, cost-effective methods [9]. Refractivity-from-clutter (RFC) is proposed to address these requirements in near-real time [10]–[12]. It is a self-contained remote sensing method for refractivity inversion which potentially outperforms other refractivity estimation techniques [13], [14].

The current objective of RFC is to invert refractivity from sea-surface reflected radar clutter typically under 10 minutes with high reliability in realistic high-dimensional scenarios [15], [16]. Commonly, the inversion problem is formulated as a simulation-driven nonlinear optimization problem [13]. Computationally-efficient simulation methods exist solving parabolic equations with split-step techniques [17], [18]. The inversion technique [13] and the clutter model [19] are scenario-dependent open questions, however.

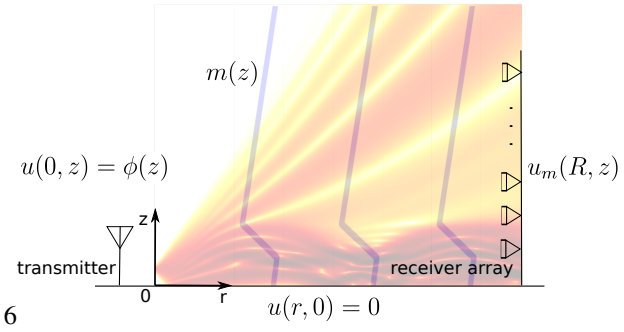

Fig. 1. An illustration of the bistatic configuration.

Inversion of refractivity from sea-reflected radar clutter or array antenna measurements, as illustrated in Figure 1, is a complex nonlinear, ill-posed problem [20]. Historically, the inversion complexity has been reduced thanks to coarse parametrization with functional representations in altitude [21], [22]. In parallel, range-independent medium is assumed [23]. Until the end of 2000s, several RFC techniques have been proposed with varying degrees of simplification on the spatial variability of refractive index (e.g., [24]–[31]). However, these techniques are not applicable for high-dimensional problems since the computational cost of inversion increases with the number of parameters to invert. Therefore, they are not efficient for problems at high frequencies when the propagation becomes increasingly sensitive to the spatial details of the medium inhomogeneities [13]. That is why some recent works have investigated the inversion of refractivity profiles defined using high-dimensional nonparametric functional models.

The first RFC technique whose computational cost does not depend on the number of parameter to invert has been developed in [32] in the framework of variational adjoint approach in 2010. The authors have derived the adjoint model (AM) for two-dimensional narrow-angle parabolic equation (2-D NAPE) which is solved using split-step Fourier (SSF) technique. Following studies have confirmed the severity of ill-posedness in high-dimensional scenarios despite regularization [33]–[35]. Unfortunately, today's adjoint-based RFC techniques still require unrealistically good initial guess with additional apriori information or need to incorporate dimensionality reduction techniques [36], [37]. Thus, reliable inversions which are purely driven by real-time data have not been realized yet in high-dimensional realistic configurations in 2-D. Other recent

Manuscript received Month Day, Year. This work is supported by ENAC/ISAE-SUPAERO/ONERA Research Federation.

Uygar Karabaş, ENAC, Department TELECOM-EMA, 31400 Toulouse, France – ISAE-SUPAERO, Université de Toulouse, 31400 Toulouse, France (e-mail: uygar.karabas@enac.fr).

Youssef Diouane, ISAE-SUPAERO, Université de Toulouse, 31400 Toulouse, France (e-mail: youssef.diouane@isae-supaero.fr).

Rémi Douvenot, ENAC, Department TELECOM-EMA, 31400 Toulouse, France (e-mail: remi.douvenot@enac.fr).

efforts concentrate on improving RFC in low-dimensional scenarios [38]–[42].

Despite the prominence of forward model (FM) accuracy in inverse problems, no previous study has attempted to fuse the adjoint-based approach with a wide-angle propagation model in RFC community. In this work, we extend the adjoint approach for 2-D wide angle parabolic equation (WAPE) by identifying the adjoint of square-root propagation operator. The proposed solution is validated numerically. Our main motivation is to enrich the pool of available adjoint models in radio and acoustic wave propagation communities with the most accurate WAPE on which split-step technique is applicable. We simulate the adjoint model with split-step wavelet (SSW) technique [18], which is faster than SSF, to tend towards a real-time accurate system. We aim at capturing any refractive condition at the spatial resolution of FM simulations by adopting point-by-point inversion approach in altitude [32].

Unlike previous work, the obtained gradient of the cost function is computed and validated successfully using a finite differences approximation. We also include the optimization landscapes in our analysis in order to visualize the inversion complexity and to explain how much the inversion is sensitive to initial guess for a given setup [43]. The method is presented for tomographic approach as an intermediate step towards a full effective RFC system. Although regularization techniques are kept out of scope of this work at this stage, our parametric study still shows the potential of our proposed approach.

The outline of the paper is as follows. In Section II, the formulations of our problem are presented. In Section III, the numerical methods are explained. Numerical test results are detailed in Section IV.

II. Modeling

In this section, we first give an overview of adjoint method in generic sense. After defining the forward problem and the inverse problem, the adjoint model is derived. The derivation is done in continuous adjoint form, so the parametrization and data are kept in functional forms. The recipe for the discrete adjoint formulation and finite dimensional setting of data and parametrization are explained in other appropriate sections.

A. Framework overview

In this section, the inverse problem framework is presented following [44] to put forward the motivation. The inverse problem is seen as the minimization of a square error functional over control parameter m in the bounded admissible space M_{ad} given by:

$$\min_{m\in M_{\text{ad}}} J(m) = \frac{1}{2}\left\|d_m^{\text{sim}} - d^{\text{obs}}\right\|_D^2. \tag{1}$$

The cost function $J(m)$ depends on the parameter m through the simulated measurement d_m^{sim}. The observation state d^{obs} is an experimental measurement function. We seek for a solution using an efficient gradient-based optimization method. For that reason, we choose to work with the square error functional (1) as this norm is differentiable. We present the standard formalism to obtain the gradient of the cost function below.

Consider the inverse problem (1) where $D = L^2(\Gamma_R)$ and Γ_R forms a partition of the domain Ω. The map of misfit quantification is given by:

$$\begin{aligned} K &: D \to \mathbb{R}, \\ d &\mapsto K(d) = \frac{1}{2}\left\|d - d^{\text{obs}}\right\|_D^2 .6 \end{aligned} \tag{2}$$

The simulated measurements d_m^{sim} are taken via an observation operator P that applies to the the state $u_m \in U = L^2(\Omega)$, i.e., $u_m \mapsto d_m^{\text{sim}} = P(u_m)$. The state u is uniquely defined for a given parameter m with the state equation $F(u,m) = 0$ at $u = u_m$. This latter is calculated from m using the forward map S:

$$\begin{aligned} S &: M_{\text{ad}} \to U, \\ 6m &\mapsto u_m = S(m) \text{ such that } F(u_m, m) = 0. \end{aligned} \tag{3}$$

Note that the cost function J is a composite function given by $J(m) = K \circ P \circ S(m)$. The gradient of J with respect to m is given by [44]:

$$\nabla_m J = \phi'(m)^* \nabla_{u_m} J, \tag{4}$$

where $\phi(m) = P \circ S(m)$ and $\phi'(m)$ is the differential of the mapping $\phi(m)$. The asterisk * denotes its adjoint. The function $\nabla_{u_m} J$ is the forcing function of the adjoint model [45]. Since ϕ is implicitly defined with the solution of the state equation, the implementation of (4) is not straightforward in our case. Therefore, we cast (4) using the variational form in order to obtain an explicit adjoint equation which allows the gradient to be identified and to be calculated more simply. In the following sections, the elements given in this section are specified for our particular problem.

B. The forward problem

This section discusses the physical modeling part in the adjoint formalism given by (3). In the context of propagation at open-sea environment with azimuthal symmetry, modeling of electromagnetic wave propagation considers solely forward propagating part of the Helmholtz equation in cylindrical coordinates:

$$\partial_r u - jk_0\left(1 - Q\right)u = 0, \tag{5}$$

which is also called the one-way equation. The square-root operator Q is given by $Q = \sqrt{m^2(z) + k_0^{-2}\partial_z^2}$ with k_0 the wave number in vacuum and $m(z) \in \mathbb{R}_+$ the modified refractive index that accounts for earth roundness. Equation (5) is exact for range-independent medium as long as the far field approximation holds, and takes into consideration the entire forward propagating wave field propagating at frequency $f = k_0 c/2\pi$. The reduced field $u(r,z) \in \mathbb{C}$ is related to the power at the receiver antenna by taking into account the distance, antenna gain and medium impedance [46].

There are numerous choices to model the propagation in the lower troposphere depending on how accurate Q is approximated in (5) [46], [47]. The standard parabolic approximation (NAPE) is the first order approximation of Q [48], it has limited accuracy [49] and it is the only model used in adjoint-based RFC systems so far [32]–[37]. In this paper, we use the

wider angle approximation (WAPE) as forward model, which is introduced by Thomson and Chapman [50] for underwater acoustics according to the splitting of Q as proposed by Feit and Fleck [51]:

$$\partial_r u + j\left[k_0(m(z)-1) + \left(\sqrt{k_0^2+\partial_z^2} - k_0\right)\right]u = 0, \tag{6a}$$

$$u(0,z) = \phi(z), \tag{6b}$$

$$u(r,0) = 0. \tag{6c}$$

This model considers the boundary condition of a flat perfectly-electric-conducting surface at $z = 0$ with source term $\phi(z)$ modeling the initial field of emitted radio waves at horizontal polarization. Note that the state equation (6a) could also take into account a dielectric ground using a variable change proposed by [17]. However, reflection coefficient $c_R = -1$ is a good approximation for both polarizations at very grazing angles.

To sum up, the forward problem is to determine the state u_m for a given parameter model m by solving (6).

C. The inverse problem

In our inverse problem, we target to determine the parameter model m that minimizes the following cost function:

$$\min_{m\in M_{\text{ad}}} J(m) = \frac{1}{2}\int_0^Z \left|d_m^{\text{sim}} - d^{\text{obs}}\right|^2 dz. \tag{7}$$

The problem (7) is designed with some idealizations which help the validation of the inversion process. Namely, for an objective refractivity model m_{OBJ}, the experimental measurements will be synthetically generated using the forward model (6). According to the tomographic approach given in Figure 1, the measurements are taken at the range $r = R$ such that $P : u(r,z) \mapsto |u(R,z)|^2$ and data space D is such that $\Gamma_R = \{R\} \times [0, Z]$. Therefore, the observed data obey $d^{\text{obs}} = \{|u(R,z)|^2 : F(u, m_{\text{OBJ}}) = 0\}$. In our study, the parameter model m is function of altitude z only. Note that $d^{\text{obs}} \in \text{Im}(P \circ S)$ so the existence of global minimum is guaranteed for (7). But some other solutions become indistinguishable from m_{OBJ} since phase is immeasurable.

In a realistic scenario, simulated measurement with (6) would not perfectly produce the experimental measurement. The ground is modeled better as dielectric ground. The refractivity varies with range. In addition, measurements are time-averaged, contain noise and cannot be pointwised in practice. Modelling and measurement errors will add to the complexity of the idealized inverse problem. Therefore, it is of interest to avoid real-world data during validation of the inversion routine.

We note also that noise needs to be added to synthetic measurements in order to assess the robustness of the inversion algorithm against instabilities. Here, the noise modeling does not aim to be realistic and the inversion results from noisy data are neither an indicator of performance in real operation nor conclusive. Instead, the aim is to deduce the sensitivity of solver of (7) to perturbations. In order to be able to draw conclusion from inversion of noise-free synthetic data, it is necessary to show a certain level of robustness to noise. In that context, additive Gaussian noise can be added to the simulated measurements, i.e.,

$$d^{\text{obs}}_{\text{noisy}} = d^{\text{obs}} + \zeta \tag{8}$$

where ζ follows a centered normal Gaussian distribution with a standard deviation of $\tau \times \text{rms}\left(\sqrt{d^{\text{obs}}}\right)$. The function $\text{rms}(x)$ is root-mean-square of function $x \in \mathbb{R}$ and τ is termed as the level of noise in this work.

D. The tangent linear model

Let us denote $F(u_m, m) = F_m$ for brevity. Assume a linear perturbation on the parameter model in the direction $\hat{m}$ such that $F_{m+\alpha\hat{m}} = 0$. We seek for the operator F' which fulfills the following relation:

$$\lim_{\alpha\to 0} \frac{\|F_{m+\alpha\hat{m}} - F_m - F'(\hat{u}_m, m; \hat{m})\alpha\hat{m}\|}{\|\alpha\hat{m}\|} = 0. \tag{9}$$

Here, the operator F' is referred to as the Fréchet derivative of operator F. The function $\hat{u}_m \in L^2(\Omega)$ satisfies the tangent linear model (TLM) $F'(\hat{u}_m, m; \hat{m}) = 0$ and it is referred to as the Gâteaux differential of u_m with respect to $\hat{m}$:

$$\lim_{\alpha\to 0} \frac{u_{m+\alpha\hat{m}} - u_m}{\alpha} = \hat{u}_m. \tag{10}$$

Substituting the operator F with (6) in (9), one deduces that the TLM satisfies the following property:

$$\partial_r \hat{u}_m + j\left[k_0(m-1) + \left(\sqrt{k_0^2+\partial_z^2} - k_0\right)\right]\hat{u}_m + jk_0\hat{m}u_m = 0 \quad \text{on } \Omega, \tag{11a}$$

$$\hat{u}_m(0,z) = 0, \tag{11b}$$

$$\hat{u}_m(r,0) = 0. \tag{11c}$$

In what comes next, for two given functions f and h, we will make use of the following inner products:

$$\begin{aligned}
\langle\!\langle f, h\rangle\!\rangle &= \int_0^Z \int_0^R f(r,z)\cdot\overline{h(r,z)}\; dr dz,\\
\langle f, h\rangle_{\mathcal{Z}} &= \int_0^Z f(r,z)\cdot\overline{h(r,z)}\; dz,\\
\langle f, h\rangle_{\mathcal{R}} &= \int_0^R f(r,z)\cdot\overline{h(r,z)}\; dr,
\end{aligned} \tag{12}$$

where $\bar{h}$ is the complex conjugate of h. We also note that

$$\langle\!\langle f, h\rangle\!\rangle = \int_0^R \langle f, h\rangle_{\mathcal{Z}}(r)\; dr = \int_0^Z \langle f, h\rangle_{\mathcal{R}}(z)\; dz. \tag{13}$$

E. Gradient of the cost function

The gradient $\nabla_m J$ of the cost function J, at the parameter model m, can be obtained using the fact that:

$$J'(m;\hat{m}) = \langle \nabla_m J, \hat{m}\rangle_{\mathcal{Z}}, \tag{14}$$

where $J'(m;\hat{m})$ is the Gâteaux differential of $J(m)$ with respect to $\hat{m}$, i.e.,

$$J'(m;\hat{m}) = \lim_{\alpha\to 0} \frac{J(m+\alpha\hat{m}) - J(m)}{\alpha}. \tag{15}$$

Then, the gradient of the cost function (7) is given by the following:

$$\begin{aligned}\langle\nabla_m J, \hat{m}\rangle_{\mathcal{Z}} &= J'(m;\hat{m}) \\ &= 2\int_0^{\mathcal{Z}} \Re\left\{\left(|u_m(R,z)|^2 - d^{obs}\right) u_m(R,z)\cdot\overline{\hat{u}_m(R,z)}\right\} dz \\ &= 2\Re\left\{\left\langle\left(|u_m(R,z)|^2 - d^{obs}\right) u_m(R,z), \hat{u}_m(R,z)\right\rangle_{\mathcal{Z}}\right\},\end{aligned} \tag{16}$$

where $\Re\{x\}$ denotes the real part of $x \in \mathbb{C}$.

F. The adjoint model

The gradient $\nabla_m J$ is defined by deriving the adjoint state equation F'^* from the variational form of F'. A unique adjoint state $w_m(r,z) \in \mathbb{C}$ exists such that $\langle\!\langle w_m, F'(\hat{u}_m, m; \hat{m})\rangle\!\rangle = 0$ which (16) is subject to. Let us drop index m from the function w_m, u_m and $\hat{u}_m$ for brevity. The variational form is:

$$\begin{aligned}&\langle\!\langle w, \partial_r \hat{u}\rangle\!\rangle + \langle\!\langle w, jk_0(m-1)\hat{u}\rangle\!\rangle \\ &+ \langle\!\langle w, j((k_0^2 + \partial_z^2)^{1/2} - k_0)\hat{u}\rangle\!\rangle + \langle\!\langle w, jk_0\hat{m}u\rangle\!\rangle = 0.\end{aligned} \tag{17}$$

Applying the rule of partial integration considering (11b) and (11c) leads to the following variational problem:

$$\begin{aligned}&-\langle\!\langle \partial_r w, \hat{u}\rangle\!\rangle + \langle w, \hat{u}\rangle_{\mathcal{Z}}|_{r=R} - \langle\!\langle jk_0(m-1)w, \hat{u}\rangle\!\rangle \\ &- \langle\!\langle j((k_0^2 + \partial_z^2)^{1/2} - k_0)^* w, \hat{u}\rangle\!\rangle - \langle\!\langle jk_0 w\overline{u}, \hat{m}\rangle\!\rangle = 0.\end{aligned} \tag{18}$$

Let $A = k_0^2 + \partial_z^2$, then according to [52, Theorem 1], for any positive self-adjoint operator $A \in \mathcal{L}(H_D, H_R)$ where H_D, H_R are two Hilbert spaces, there exists a self-adjoint square root operator $\sqrt{A} = \sqrt{A}^*$. In our context, self-adjointness $A = A^*$ always holds but positiveness $\langle\!\langle Af, f\rangle\!\rangle \geq 0$ is reserved for when $\langle\!\langle \partial_z^2 f, f\rangle\!\rangle \leq \langle\!\langle k_0^2 f, f\rangle\!\rangle$. The latter indeed holds for the entire propagating modes of (6a) [46]. Thus, $\sqrt{A}^* = \sqrt{A}$ holds as far as the scope of resolution is restricted on the propagating part of the field. Since we only measure the propagating part of the field for refractivity inversion, self-adjointness of the square-root operator can be asserted in the context of RFC. Numerically this corresponds to $\Delta z \geq \lambda/2$ where Δz is the step size in the axial direction of Ω and λ is the wavelength. Consequently, we have:

$$\begin{aligned}&-\langle\!\langle \partial_r w, \hat{u}\rangle\!\rangle + \langle w, \hat{u}\rangle_{\mathcal{Z}}|_{r=R} - \langle\!\langle jk_0(m-1)w, \hat{u}\rangle\!\rangle \\ &- \langle\!\langle j((k_0^2 + \partial_z^2)^{1/2} - k_0)w, \hat{u}\rangle\!\rangle - \langle\!\langle jk_0 w\overline{u}, \hat{m}\rangle\!\rangle = 0.\end{aligned} \tag{19}$$

Observing the self-adjointness of the operators in the variational form, the aim is to derive an adjoint state equation which is the same as (6a) so that the FM solver can be inherited for AM. Combine (16) and (19). Let w_m be given by:

$$\partial_r w_m + j\left[k_0(m-1) + \left(\sqrt{k_0^2 + \partial_z^2} - k_0\right)\right] w_m = 0, \tag{20a}$$

$$w_m(R,z) = 2\left(|u_m(R,z)|^2 - d^{obs}\right) u_m(R,z), \tag{20b}$$

$$w_m(r,0) = 0, \tag{20c}$$

such that (21) holds

$$\nabla_m J = \Re\left\{jk_0 \int_0^R w_m(r,z)\cdot\overline{u_m(r,z)}\, dr\right\}. \tag{21}$$

The estimation of such gradient will now enable us to use gradient-based optimization methods (e.g., Quasi-Newton methods) which are suitable for large-scale inversion problems. In the next section, we give the implementation details for (20) and (21) and present an approach to validate both the derivation and the implementation.

III. Numerical Methods

A. Inversion strategy

The inversion process starts from an initial guess m_{IG} which gives simulated measurement data d_m^{sim} using propagation model (6). Next, the adjoint equation (20a) is solved in order to estimate the gradient using (21). The iteration parameters are estimated with a gradient-based minimization algorithm, which may include inner cost function estimations using the propagation model. The same process continues until a convergence criteria is met. In our study, we do not have access to measurements. Therefore, we generate the measurements d^{obs} synthetically using the forward model given by (6) for a known objective refractivity profile m_{OBJ}. The workflow given in Figure 2 summarizes the inversion strategy and the used notations. Next section presents the numerical methods which we use.

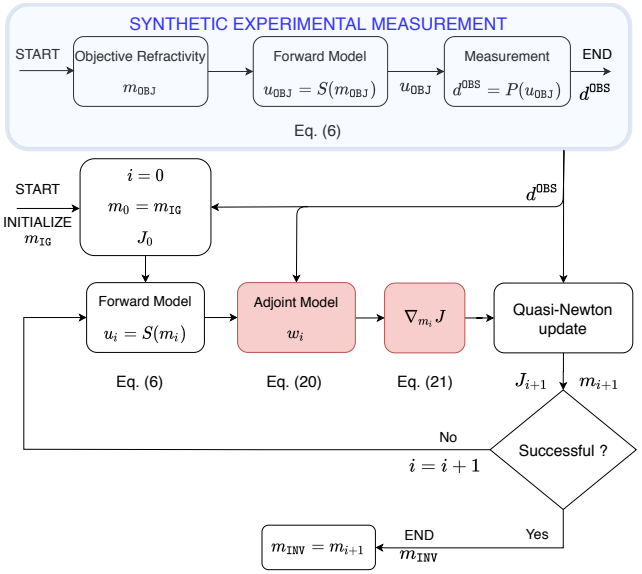

Fig. 2. Schematic of inversion workflow. The algorithm corresponding to the red boxes will be validated.

B. Numerical Methods

The forward problem (6) is modeled using SSW technique. This forward solver implementation has been validated [18]. The adjoint model solver is derived from the forward model solver where the adjoint initial condition is achieved by replacing (6b) with (20b) in the FM solver. Adjoint backpropagation is achieved by changing sign of range step from Δr to $-\Delta r$ and 180° rotation of computational domain around axial direction in the FM solver. This change of sign occurs in the free-space propagator, boundary condition and phase screen operators in [18]. The cost function (7) and its gradient (21) are computed using Simpson's rule of integration. The optimization algorithm is the well-known BFGS quasi-Newton method [53].

C. Validation of the gradient estimation

The problem (7) is difficult to solve accurately. The inversion results cannot be used for validating the quality of the work except for oversimplified cases (e.g., [54]). Therefore, it is necessary to perform a validation process starting from checking the gradient computation. This process can be seen as an intermediate step towards understanding why RFC may fail. In fact, ill-posedness in RFC can be incriminated only after running the validation process of the gradient.

The part of the inversion algorithm lacking validation is shown in the workflow in Figure 2 in red. Typically, for inverse problems, the adjoint model can be validated with dot-product test or by comparison of $\nabla_m J_{\text{AM}}$ (i.e., $\nabla_m J$ estimated using (21)) with a reference estimation of the gradient. In the context of inverse problems, the validation scope of the latter is slightly wider than that of dot-product test. If the adjoint state w_m is formulated and simulated properly, $\nabla_m J_{\text{AM}}$ would match the gradient computed with a reference method. The reference estimation of the gradient can be obtained using a finite differences (FD) scheme. Typically, for a number n of inversion parameters, the i^{th} component of the FD approximation of the gradient is given by

$$[\nabla_m J_{\text{FD}}]_i = \frac{J(m + \epsilon \boldsymbol{e}_i) - J(m)}{\epsilon}, \tag{22}$$

where $\boldsymbol{e}_i$ is the n-sized column vector whose ith component is one while all the others are zeros, and ϵ is chosen as 10^{-6}. Note that the estimation of the gradient with a finite differences scheme requires $n+1$ evaluations of the cost function, while $\nabla_m J_{\text{AM}}$ is computed at the cost of 2 FM runs [44].

To sum up, the gradients $\nabla_m J_{\text{FD}}$ and $\nabla_m J_{\text{AM}}$ should follow each other if the adjoint field is formulated properly in (20a) and simulated properly and the numerical integration of (21) is done properly. The baseline computational setup of the validation process is given in Section IV-A which also contains some notes on the validation methodology. Numerical validation is given in Section IV-C.

D. Landscapes of the cost function

There is no general technique to tackle a nonlinear inverse problem [44], [55]. Solving such a problem requires the development of a special strategy tailored for the specificity of the regarded problem.

We are asked to find the global minimum of an error functional. Some of the difficulties in adjoint-based RFC are listed as sensitivity to initial guess [35], loss of signal at long ranges [32], failure of some regularization techniques [33], insufficiency of measurement data [32], high-dimensionality [36]. The difficulties are commonly seen as a consequence of nonlinearity and ill-posedness. In practice, the two attributes reflect on the problem (7) as nonconvexity and nonsmoothness of the optimization landscape. Therefore, from our perspective, looking at the cost function landscape [43] can guide the community to build the right strategy. RFC is much more complex than (7), so optimization landscape analysis of (7) is valuable as an intermediate step for understanding why RFC is still an open problem.

In this work, we limit our analysis to two different one-dimensional optimization landscapes of the high-dimensional problem. They allow to visualize the cost function around some given solutions with a one-dimensional variation. Firstly, we define:

$$\begin{aligned} &\alpha \mapsto J(m_1(\alpha)),\ \alpha \in [-2, 2], \\ &\text{with } m_1(\alpha) = m_{\text{OBJ}} + \alpha(m_0 - m_{\text{OBJ}}). \end{aligned} \tag{23}$$

By varying the parameter model using m_1, we construct the cost function landscape around the objective refractivity profile. Secondly, we define:

$$\begin{aligned} &\alpha \mapsto J(m_2(\alpha)),\ \alpha \in [-1, 1], \\ &\text{with } m_2(\alpha) = m_0 + \alpha \left\| m_{\text{max}} - m_0 \right\|_\infty \frac{\nabla_{m_0} J}{\left\| \nabla_{m_0} J \right\|_\infty}, \end{aligned} \tag{24}$$

where m_{max} is the maximum bound in the admissible space. The landscape using the parameter model m_2 is constructed around the initial guess in the direction of the gradient. The two landscapes will be plotted and commented in Section IV-D.

IV. Numerical Analysis

In this section, firstly, the baseline computational setup is presented. Next, a parametric study is performed. After validation of the method, the inversion difficulty is explained with the directional cost function landscapes. The analysis ends with displaying the impact of initial guess on inversion and perturbation robustness tests.

A. Computational setup

In the baseline computational setup, the geometry of the computational domain Ω is a two dimensional plane constructed on axial and radial directions as given in Figure 1. The geometry is truncated such that $\Omega = [0, R] \times [0, Z]$. Altitude of interest Z is limited to 150 m. Range of propagation R is considered at different values $\in \{1, 5, 10, 30, 60\}$ km.

The mesh of discretized domain Ω_{N_r, N_z} is a uniform grid. The parameter N_r and N_z are the number of grid points along the directions $\hat{r}$ and $\hat{z}$, respectively. The cell size in altitude is set to $\Delta z = 1$ m for all cases. The cell size in range Δr is determined such that $N_r = 101$ is satisfied when $\Delta r < 100$ m, otherwise the cell size is fixed at $\Delta r = 100$ m for the control of numerical error.

The initial condition $\phi(z)$ is obtained from a complex-point source positioned at $(r_s, z_s) = (-100 \text{ km}, 25 \text{ m})$. It has width of 5 m and emission frequency $f_s = 2$ GHz at horizontal polarization. This setting yields a $\phi(z)$ profile with full shape, which is useful for validation [54]. The ground is accounted with the local image method [18] and a Hanning absorbing window is applied on the top of the domain.

The refractivity is given with the modified parameter $M(z) = (m(z) - 1) \times 10^6$. The parameter M which corresponds to d^{obs} is called the objective of the inversion and denoted by M_{OBJ}. Similarly, the initial guess and the inversion result parameters are denoted by M_0 and M_{INV}, respectively. There is no variation of M with range. The simulations take into account the discretized parameter vector with dimension

$M \in \mathbb{R}^{N_z}$ using linear projection of M at grid nodes. To be clear, the aim is to invert $N_z = 151$ refractivity parameters with 151 simulated data sample from 151 experimental data sample. In this scenario, there are 151 receivers on the receiver array extending from ground level to the altitude of interest $Z = 150$ m, with the receiver spacing of Δz.

The objective refractivity $M_{\text{OBJ}}(z)$ has a trilinear structure of surface based ducts [22]. The duct is given by the following altitude-refractivity tuple: $(z, M_{\text{OBJ}}(z)) = \{(0, 330.0), (50, 350.0), (100, 330.0), (150, 335.90)\}$. The initial guess is constant at $M_0 = 330.0$ in the baseline setup.

In the next section, we give the inversion results of the workflow given in Figure 2 at different ranges for the baseline computational setup. The objective and initial guess fields are given in Figure 3 with their difference.

B. Results: inversion

The inversion routine given in Figure 2 is tested for its capability to retrieve M_{OBJ} from the corresponding measurement.

Measurement range R has an influence on inversion. The dependence of M_{INV} (the inverted refractivity model) on varying range R is given in Figure 4. One can see that it may not be possible to retrieve M_{OBJ} but M_{INV} captures the synoptic structure of M_{OBJ} at $R = 1$, 5, and 10 km with varying degrees of success. The refractivity gradient is retrieved thanks to the fact that the solution of (7) is not unique but with some dispersion in M_{INV} due to ill-posedness of (7). For $R = 30$ and 60 km, M_{INV} stays closer to the initial guess M_{IG} for increasing R. As failure of the inversion and stocking of M_{INV} around M_{IG} are progressive with the increase of R, we conclude that (7) gets more nonlinear with R.

The mechanisms of nonlinearity are the propagation model, ground reflections and dimensionality of the problem. Firstly, (7) is driven by the simulations of (6a) in which the relation between m and $u_m(R, z)$ is nonlinear. Secondly, range R matters due to multipath interference of ducted and reflected field which increasingly complicates the shape of $u_m(R, z)$ at long distances. Thirdly, nonlinearity of the problem increases with the number of parameters to invert. Thus, the number of local minima on the optimization landscape increases. The problem (7) becomes such that a local minima can be found in the neighbourhood of initial guess for $R = 60$ km with 151 optimization parameters.

Even so, we need to verify that the gradient is computed successfully and this complexity phenomenon is driven by the cost function landscape. To achieve this, firstly, we perform the validation with finite differences at different ranges as described in Section III.

C. Results: validation of the gradient

Since the inversion could not retrieve M_{OBJ}, we first put into question the validity of adjoint model. In this section, the adjoint model (20) presented in Section II-F is validated with the comparison of $\nabla_m J_{\text{FD}}$ and $\nabla_m J_{\text{AM}}$.

We validate over the gradient of the first descent iteration. AM estimates the gradient that would otherwise have to be computed using FD at higher cost. In Figure 5, the gradient calculated with the AM and with FD are plotted with respect to altitude for the different values of R. Both gradients perfectly match, except that at $R = 1$ km there exists some differences due to the very low value of the gradient. Thus the gradient estimation is more robust for long range applications.

Numerical issues become prominent in the computation of the gradient when the gradient is low as in Figure 5a. For AM, this occurs when w approaches to null and gradient is estimated near a stationary point according to (20b) and (21). For FD this corresponds to the case where field bending effect of different m is not significant on $|u|$, according to (22), which is expected at short ranges. Thus, stationarity check is recommended for RFC applications at the end of inversion.

Consequently, the adjoint model is validated with the comparison of the gradient with FD. Failure to invert is not due to the adjoint model. Problem (7) is ill-posed within its nature even without measurement noise, modeling and theoretical errors. Potentially, the ill-posedness could be combined with convergence issues which could be included in a future work.

We have proven that the inversion does not fail due to miscomputation of the gradient. Indeed, the gradients may indicate higher ill-posedness due to removal of the phase from synthetic data [54]. Therefore, we are interested in visualizing the extent of non-convexity in the inverse problem. In the next section, this is performed for two different 1-D parametrizations to give an idea about the complexity of inversion, which may give an idea about the sensitivity to initial guess with increasing range of propagation.

D. Results: cost function landscape

Since the method is validated, we suspect that the difficulty to invert originates from the problem (7) itself. We have evidence that the difficulty increases with range according to Figure 4 so sensitivity to initial guess must also increase and more local minima are expected to appear on a rougher optimization landscape.

In Figure 6, we plot the directional cost function landscape for M_1 ((7) for model (23)) for three ranges. The increasing complexity with range can be observed as the convexity of the landscapes decreases with R. Note that M_{OBJ} is located at $\alpha = 0$ and M_{IG} at $\alpha = 1$ on this landscape. The functional (7) between M_{IG} and M_{OBJ} becomes nonconvex with R. Thus M_{IG} is more likely to be attracted to emerging local minima in its neighbourhood with gradient based optimization method.

Attention must be paid to the dimensionality of the problem when interpreting Figure 6 and 7. There are infinitely many 1-D line cuts in 151-D hypercube and indications of nonlinearity and ill-posedness can be hidden at some other line cuts. For example at 10 km, ill-posedness of (7) is obvious in M_{INV} of Figure 4c but J is quasiconvex in 6b for $\alpha \in [0, 1]$. Nevertheless, one can deduce from Figure 6 that better initial guess is needed to successfully invert at long ranges. Otherwise, the optimization gets trapped at a local minimum as landscape over 151-D hypercube is expectedly more rough. Also note that the landscapes with the standard atmosphere as the initial guess (not presented here) are similar to Figure 6.

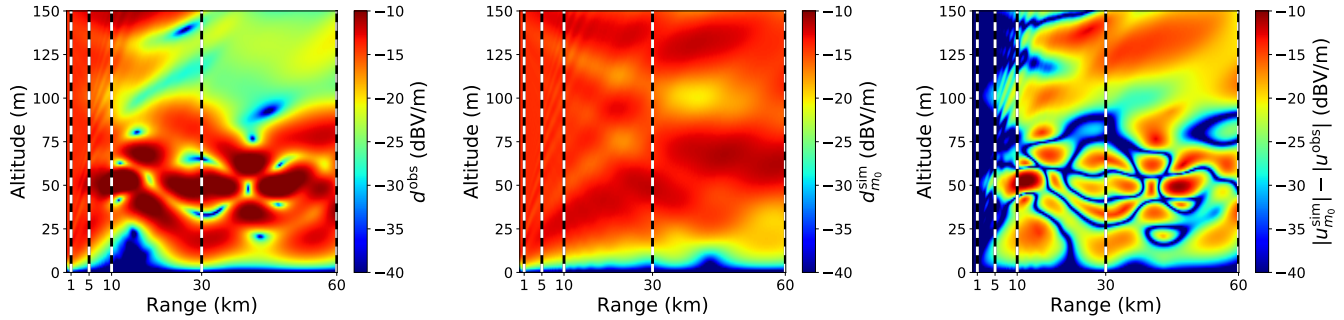

(a) Synthetically-generated measured field. (b) Simulated field for initial guess. (c) Absolute error between simulated and measured fields.

Fig. 3. Propagating fields at different range R.

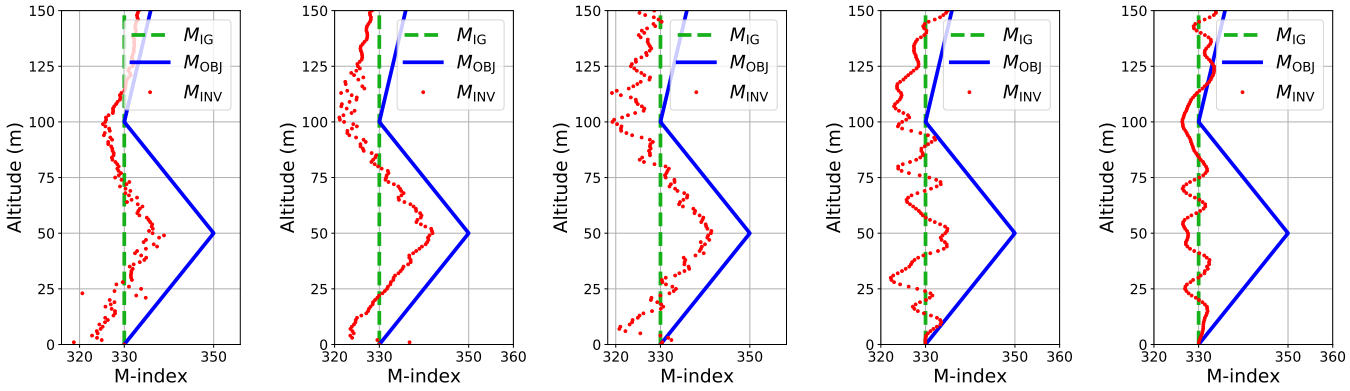

(a) $R = 1$ km. (b) $R = 5$ km. (c) $R = 10$ km. (d) $R = 30$ km. (e) $R = 60$ km.

Fig. 4. Inverted parameters at different range R.

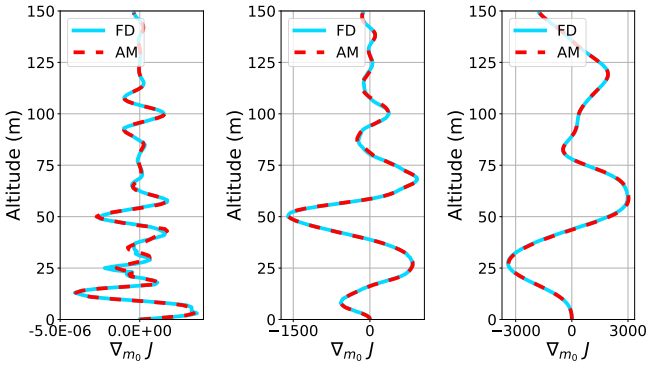

(a) $R = 1$ km. (b) $R = 10$ km. (c) $R = 60$ km.

Fig. 5. Validation of the gradient for the first descend iteration. Comparison of the gradient $\nabla_{m_0} J_{\text{FD}}$ computed with finite differences (FD) method vs. $\nabla_{m_0} J_{\text{AM}}$ computed with adjoint model (AM). Relative $L2$ error of these estimations are 13.2%, 3.2% and 1.8% respectively.

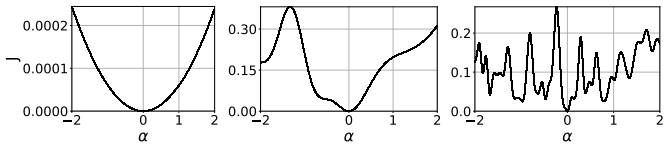

(a) $R = 1$ km. (b) $R = 10$ km. (c) $R = 60$ km.

Fig. 6. Obtained landscape for the function $\alpha \to J(m_1(\alpha))$ at different range R, see (23).

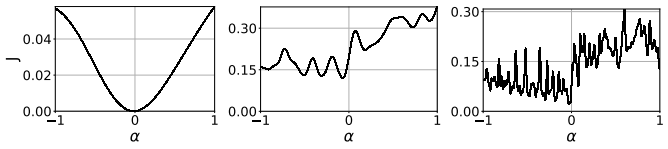

(a) $R = 1$ km. (b) $R = 10$ km. (c) $R = 60$ km.

Fig. 7. Obtained landscape for the function $\alpha \to J(m_2(\alpha))$ at different range R, see (24).

The analysis is enriched with the landscape drawn at the direction of the gradient according to (24) as given in Figure 7. Note that M_{IG} is located at $\alpha = 0$ on this landscape. The functional (7) has more local minima on this 1-D view when compared to Figure 6. Again, it is more difficult to invert at long ranges because the optimization landscape becomes more nonconvex. In the next section, we expand our analysis with inversions by using different initial guesses.

E. Results: impact of initial guess

Sensitivity of optimization to initial guess may appear when a nonlinear problem is solved with gradient-based methods. A good initial guess can significantly improve inversions by diminishing the undesirable effects of nonlinearity and ill-posedness. In this section, the aim is to check if we can observe some improvement with different initial guesses and if the conclusions made in the results section are reasonable for other initial guesses as well.

In Figure 8, we present the inverted parameters in altitude for different initial guesses at $R = 10$ km, in order to show examples of how an initial guess could improve or worsen the inversion. Firstly in Figure 8a, M_{IG} is set at closer to M_{OBJ} than in Figure 4c and the inversion improves. Without showing more figures, we comment that a detailed study of this case revealed that M_{INV} exhibits further self-regularization with the further improvement of M_{IG} towards M_{OBJ} and the gradient information is retrieved more smoothly. Next, Figures 8b and 8d show that a ducting condition in the initial guess significantly improves the inversion of a ducting condition, even if both initial guesses are linear with altitude. Another scenario is simulated in Figure 8c. It mimics conditions for which short-time history or meteorological input is available as initial guess. The inversion managed to track the assumed temporal variation nearly-successfully. Note that M_{IG} and M_{OBJ} have the same duct strength in in this example, Figure 8c.

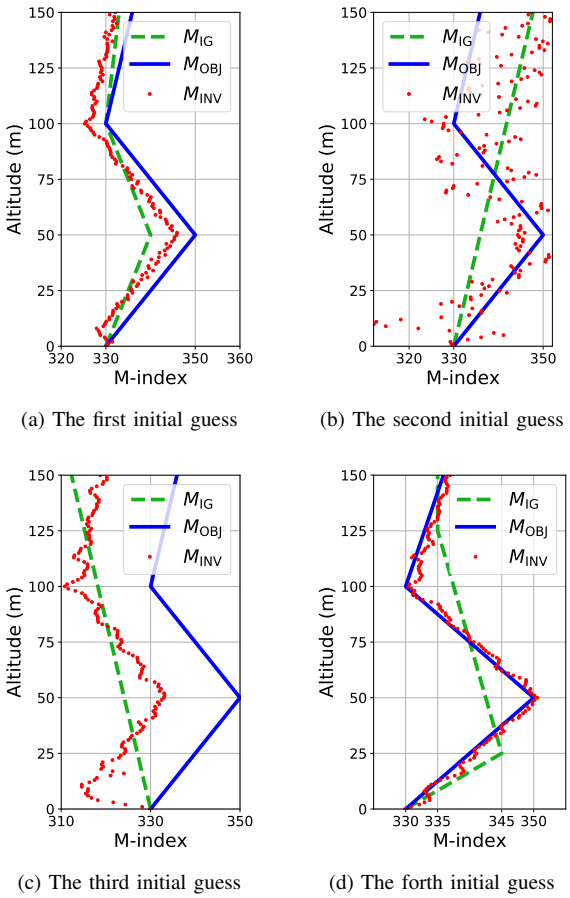

(a) The first initial guess (b) The second initial guess

(c) The third initial guess (d) The forth initial guess

Fig. 8. Inversion at $R = 10$ km for different initial guesses.

F. Results: noise impact and robustness test

It is necessary to show that the inversions are robust to noise (see II-C for details). The motivation is to see if the conclusions made without noise are reasonable in the presence of perturbations on data. If our system is robust, it should be insensitive to small perturbations or precision errors on data; this increases confidence in the inversion results. Robustness test is performed at $R = 10$ km with different levels of noise τ on measurements according to (8).

In Figure 9, we present the inverted parameters in altitude for different noise level τ at $R = 10$ km. The inversions naturally become more ill-posed with the addition of noise on measurement data. The mean of the inversions seem to follow $M_{\text{INV}}|_{\tau=0}$ given in Figure 8a but dispersion of the parameters grows with τ. In this example, the inversion is resilient to 10% of perturbation on data as far as capturing of the gradient of M_{OBJ} is concerned. The inversion deviates progressively from the attraction basin of $M_{\text{INV}}|_{\tau=0}$ as $\tau > 10\%$.

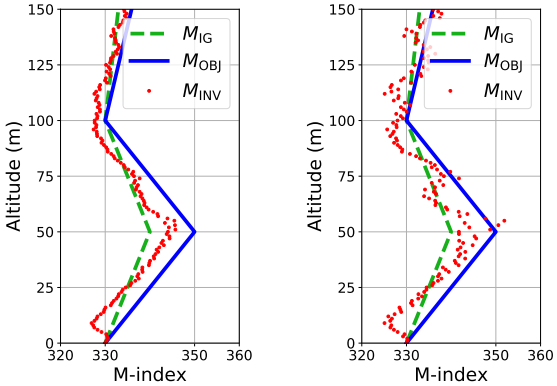

(a) $\tau = 10\%$ (b) $\tau = 50\%$

Fig. 9. Robustness at different noise level τ at $R = 10$ km.

V. Conclusion

This paper presents our attempts to predict the ambient refractive index in the troposphere. The goal is to provide real-time situational awareness for modern seaborne and airborne electromagnetic emitters under anomalous propagation conditions. The adjoint method properly addresses the high-dimensionality of the refractivity inversion for such modern detection systems and it is the backbone method on which our inversion strategy will be built. For this reason, its validation has received emphasis at the initial stage of development [54].

We attach importance to upgrade the forward model to tighten the control on inversion accuracy for this ill-posed inverse problem in real-world scenarios. Despite being hypothetical for the implications, we advocate the use of the wide-angle approximation of the parabolic equation for adjoint-based refractivity inversions because the method is available at no additional cost when compared to that of NAPE. In this paper, we show how to derive the adjoint WAPE, explain how to construct the adjoint code, and validate the adjoint model by using a finite-difference approach. Thanks to the validation of the gradient, we are sure that it is the ill-posedness of the regarded inverse problem that leads to failure of inversion. We explain this failure with nonconvexity of directional cost function landscapes and high-dimensionality of the problem. Since the gradient-based method which we use is prone to be attracted to local minimum during iterations, the increasing sensitivity to initial guess with range can be inferred from the cost function landscape. This latter is seen to lose convexity with distance, as the problem becomes more nonlinear.

The parameter study shows the potential use of this method as a gradient retrieval system. In this study, we have obtained acceptable results until around 10 km range. We have also verified the validity of our assessments using different initial guesses. The ducting initial conditions are found to work better as initial guesses for the regarded objective refractivity profile. The proposed method is shown to be robust for small Gaussian perturbations in the measurements.

More detailed analyses are necessary to assess the performance prediction quality of the emitters. Nevertheless, it is inspiring to obtain some sort of gradient retrieval with our validated basic strategy. We have to note that the problem is expectedly more ill-posed in real world scenarios due to measurement and modeling errors. Our next step will be to investigate multiscaling strategies [56] and regularization techniques [57] to deal with inversion at long-distance and more realistic high-dimensional scenarios.

ACKNOWLEDGMENT

This work is part of activities of ENAC/ISAE-SUPAERO/ONERA research federation.

REFERENCES

[1] H. V. Hitney, "Integrated refraction effects prediction system (IREPS)," *Naval Engineers Journal*, vol. 88, no. 2, pp. 257–262, 1976.

[2] M. I. Skolnik, *Introduction to Radar Systems*, 3rd ed. McGraw-Hill New York, 2001.

[3] G. Baumgartner, H. Hitney, and R. Pappert, "Duct propagation modelling for the integrated-refractive-effects prediction system (IREPS)," in *IEE Proceedings F (Communications, Radar and Signal Processing)*, vol. 130, no. 7. IET, 1983, pp. 630–642.

[4] W. L. Patterson, "Advanced refractive effects prediction system (AREPS)," in *2007 IEEE Radar Conference*. IEEE, 2007, pp. 891–895.

[5] G. D. Dockery, S. A. Ra'id, D. E. Freund, J. Z. Gehman, and M. H. Newkirk, "An overview of recent advances for the TEMPER radar propagation model," in *2007 IEEE Radar Conference*. IEEE, 2007, pp. 896–905.

[6] Y. Hurtaud, J. Claverie, E. Mandine, and M. Aidonidis, "Une préfiguration des futures aides tactiques: filecode PREDEM: Observation des côtes et des océans: Senseurs et Systèmes (OCOSS)," *Rev. Electr. Electron*, pp. 31–41, 2008.

[7] *TERPEM User Guide*, 2nd ed., Signal Science Ltd. Abingdon, UK, 2005.

[8] R. Douvenot, V. Fabbro, P. Gerstoft, C. Bourlier, and J. Saillard, "A duct mapping method using least squares support vector machines," *Radio Science*, vol. 43, 2008.

[9] H. V. Hitney, J. H. Richter, R. A. Pappert, K. D. Anderson, and G. B. Baumgartner, "Tropospheric radio propagation assessment," *Proceedings of the IEEE*, vol. 73, no. 2, pp. 265–283, 1985.

[10] J. Krolik and J. Tabrikian, "Tropospheric refractivity estimation using radar clutter from the sea surface," in *Proceedings of the 1997 Battlespace Atmospherics Conference, SPAWAR Syst. Command Tech. Rep*, vol. 2989, 1998, pp. 635–642.

[11] J. L. Krolik, J. Tabrikian, A. Vasudevan, and L. T. Rogers, "Using radar sea clutter to estimate refractivity profiles associated with the capping inversion of the marine atmospheric boundary layer," in *IEEE 1999 International Geoscience and Remote Sensing Symposium. IGARSS'99 (Cat. No. 99CH36293)*, vol. 1. IEEE, 1999, pp. 649–651.

[12] L. T. Rogers, C. P. Hattan, and J. K. Stapleton, "Estimating evaporation duct heights from radar sea echo," *Radio Science*, vol. 35, no. 4, pp. 955–966, 2000.

[13] A. Karimian, C. Yardim, P. Gerstoft, W. S. Hodgkiss, and A. E. Barrios, "Refractivity estimation from sea clutter: An invited review," *Radio Science*, vol. 46, pp. 1–16, 2011.

[14] C. Yardim, "Statistical estimation and tracking of refractivity from radar clutter," Ph.D. dissertation, UC San Diego, 2007.

[15] L. T. Rogers, "Effects of the variability of atmospheric refractivity on propagation estimates," *IEEE Transactions on Antennas and Propagation*, vol. 44, no. 4, pp. 460–465, 1996.

[16] R. Douvenot, V. Fabbro, C. Bourlier, J. Saillard, H.-H. Fuchs, and H. Essen, "Refractivity from sea clutter applied on vampira and wallops' 98 data," in *2008 International Conference on Radar*. IEEE, 2008, pp. 482–487.

[17] D. Dockery and J. R. Kuttler, "An improved impedance-boundary algorithm for Fourier split-step solutions of the parabolic wave equation," *IEEE Transactions on Antennas and Propagation*, vol. 44, no. 12, pp. 1592–1599, 1996.

[18] H. Zhou, R. Douvenot, and A. Chabory, "Modeling the long-range wave propagation by a split-step wavelet method," *Journal of Computational Physics*, vol. 402, p. 109042, 2020.

[19] L. Rosenberg, S. Watts, and M. S. Greco, "Modeling the statistics of microwave radar sea clutter," *IEEE Aerospace and Electronic Systems Magazine*, vol. 34, no. 10, pp. 44–75, 2019.

[20] C. Yardim, P. Gerstoft, and W. S. Hodgkiss, "Tracking refractivity from clutter using kalman and particle filters," *IEEE Transactions on Antennas and Propagation*, vol. 56, no. 4, pp. 1058–1070, 2008.

[21] H. Dougherty and B. Hart, "Recent progress in duct propagation predictions," *IEEE Transactions on Antennas and Propagation*, vol. 27, no. 4, pp. 542–548, 1979.

[22] P. Gerstoft, L. T. Rogers, J. L. Krolik, and W. S. Hodgkiss, "Inversion for refractivity parameters from radar sea clutter," *Radio science*, vol. 38, no. 3, 2003.

[23] J. Goldhirsh and D. Dockery, "Propagation factor errors due to the assumption of lateral homogeneity," *Radio Science*, vol. 33, no. 2, pp. 239–249, 1998.

[24] J. Tabrikian, J. L. Krolik, and S. Vasudevan, "Estimating tropospheric refractivity parameters from radar sea clutter," in *Proceedings of the IEEE Signal Processing Workshop on Higher-Order Statistics. SPW-HOS'99*. IEEE, 1999, pp. 345–348.

[25] P. Gerstoft, L. T. Rogers, W. S. Hodgkiss, and L. J. Wagner, "Refractivity estimation using multiple elevation angles," *IEEE Journal of oceanic engineering*, vol. 28, no. 3, pp. 513–525, 2003.

[26] A. Barrios, "Estimation of surface-based duct parameters from surface clutter using a ray trace approach," *Radio science*, vol. 39, no. 6, pp. 1–9, 2004.

[27] C. Yardim, P. Gerstoft, and W. S. Hodgkiss, "Estimation of radio refractivity from radar clutter using bayesian monte carlo analysis," *IEEE Transactions on Antennas and Propagation*, vol. 54, no. 4, pp. 1318–1327, 2006.

[28] S. Vasudevan, R. H. Anderson, S. Kraut, P. Gerstoft, L. T. Rogers, and J. L. Krolik, "Recursive bayesian electromagnetic refractivity estimation from radar sea clutter," *Radio Science*, vol. 42, no. 2, 2007.

[29] C. Yardim, P. Gerstoft, and W. S. Hodgkiss, "Statistical maritime radar duct estimation using hybrid genetic algorithm–markov chain monte carlo method," *Radio Science*, vol. 42, no. 3, 2007.

[30] B. Wang, Z.-S. Wu, Z. Zhao, and H.-G. Wang, "Retrieving evaporation duct heights from radar sea clutter using particle swarm optimization (pso) algorithm," *Progress In Electromagnetics Research*, vol. 9, pp. 79–91, 2009.

[31] R. Douvenot, V. Fabbro, P. Gerstoft, C. Bourlier, and J. Saillard, "Real time refractivity from clutter using a best fit approach improved with physical information," *Radio Science*, vol. 45, no. 1, 2010.

[32] X.-F. Zhao, S.-X. Huang, and H.-D. Du, "Theoretical analysis and numerical experiments of variational adjoint approach for refractivity estimation," *Radio Science*, vol. 46, 2011.

[33] X.-F. Zhao and S.-X. Huang, "Refractivity from clutter by variational adjoint approach," *Progress In Electromagnetics Research*, vol. 33, pp. 153–174, 2011.

[34] X. Zhao and S. Huang, "Estimation of atmospheric duct structure using radar sea clutter," *Journal of the Atmospheric Sciences*, vol. 69, no. 9, pp. 2808–2818, 2012.

[35] ——, "Atmospheric duct estimation using radar sea clutter returns by the adjoint method with regularization technique," *Journal of Atmospheric and Oceanic Technology*, vol. 31, no. 6, pp. 1250–1262, 2014.

[36] X. Zhao, C. Yardim, D. Wang, and B. M. Howe, "Estimating range-dependent evaporation duct height," *Journal of Atmospheric and Oceanic Technology*, vol. 34, no. 5, pp. 1113–1123, 2017.

[37] X. Zhao, ""refractivity-from-clutter" based on local empirical refractivity model," *Chinese Physics B*, vol. 27, no. 12, p. 128401, 2018.

[38] V. Fountoulakis and C. Earls, "Duct heights inferred from radar sea clutter using proper orthogonal bases," *Radio Science*, vol. 51, no. 10, pp. 1614–1626, 2016.

[39] X. Zhu, J. Li, M. Zhu, Z. Jiang, and Y. Li, "An evaporation duct height prediction method based on deep learning," *IEEE Geoscience and Remote Sensing Letters*, vol. 15, no. 9, pp. 1307–1311, 2018.

[40] S. Penton and E. Hackett, "Rough ocean surface effects on evaporative duct atmospheric refractivity inversions using genetic algorithms," *Radio Science*, vol. 53, no. 6, pp. 804–819, 2018.

[41] C. Tepecik and I. Navruz, "A novel hybrid model for inversion problem of atmospheric refractivity estimation," *AEU-International Journal of Electronics and Communications*, vol. 84, pp. 258–264, 2018.

[42] M. A. Gilles, C. Earls, and D. Bindel, "A subspace pursuit method to infer refractivity in the marine atmospheric boundary layer," *IEEE Transactions on Geoscience and Remote Sensing*, vol. 57, pp. 5606–5617, 2019.

[57] G. Chavent, *Nonlinear least squares for inverse problems: theoretical foundations and step-by-step guide for applications*. Springer Science & Business Media, 2010.

[43] H. Barucq, G. Chavent, and F. Faucher, "A priori estimates of attraction basins for nonlinear least squares, with application to helmholtz seismic inverse problem," *Inverse Problems*, vol. 35, no. 11, p. 115004, 2019.

[44] M. Kern, *Numerical Methods for Inverse Problems*. John Wiley & Sons, 2016.

[45] M. Meyer and J.-P. Hermand, "Optimal nonlocal boundary control of the wide-angle parabolic equation for inversion of a waveguide acoustic field," *The Journal of the Acoustical Society of America*, vol. 117, no. 5, pp. 2937–2948, 2005.

[46] M. Levy, *Parabolic equation methods for electromagnetic wave propagation*. IET, 2000, no. 45.

[47] F. B. Jensen, W. A. Kuperman, M. B. Porter, and H. Schmidt, *Computational ocean acoustics*. Springer Science & Business Media, 2011.

[48] F. D. Tappert, "The parabolic approximation method," in *Wave propagation and underwater acoustics*. Springer, 1977, pp. 224–287.

[49] J. R. Kuttler, "Differences between the narrow-angle and wide-angle propagators in the split-step Fourier solution of the parabolic wave equation," *IEEE Transactions on Antennas and Propagation*, vol. 47, no. 7, pp. 1131–1140, 1999.

[50] D. J. Thomson and N. Chapman, "A wide-angle split-step algorithm for the parabolic equation," *The Journal of the Acoustical Society of America*, vol. 74, no. 6, pp. 1848–1854, 1983.

[51] M. Feit and J. Fleck, "Light propagation in graded-index optical fibers," *Applied optics*, vol. 17, no. 24, pp. 3990–3998, 1978.

[52] A. Wouk, "A note on square roots of positive operators," *SIAM Review*, vol. 8, no. 1, pp. 100–102, 1966.

[53] J. Nocedal and S. Wright, *Numerical Optimization*. Springer Science & Business Media, 2006.

[54] U. Karabaş, Y. Diouane, and R. Douvenot, "On the use of adjoint methods for refractivity estimation in the troposphere," in *2020 14th European Conference on Antennas and Propagation (EuCAP)*. IEEE, 2020.

[55] D. H. Wolpert and W. G. Macready, "No free lunch theorems for optimization," *IEEE transactions on evolutionary computation*, vol. 1, no. 1, pp. 67–82, 1997.

[56] Y. Diouane, S. Gratton, X. Vasseur, L. N. Vicente, and H. Calandra, "A parallel evolution strategy for an earth imaging problem in geophysics," *Optimization and Engineering*, vol. 17, no. 1, pp. 3–26, 2016.